14th International Symposium on Turbulence and Shear Flow Phenomena (TSFP14)
Heidelberg, Germany, July 28–31, 2026

REYNOLDS STRESS TRANSPORT AS RESOLVED BY INSTANTANEOUS WALL-NORMAL INTEGRALS

Tanner Ragan and Perry L. Johnson
Department of Mechanical & Aerospace Engineering
University of California, Irvine
Irvine, CA, 92697
ragant@uci.edu, perry.johnson@uci.edu

ABSTRACT

Turbulence-Resolving Integral Simulation (TRIS) is a new approach for approximating wall-bounded turbulent flows using two-dimensional (streamwise-spanwise) fields of instantaneous wall-normal integrals Ragan *et al.* (2025). This approach directly captures the large and very-large scale motions with self-sustaining turbulent dynamics using equations derived from Navier-Stokes. TRIS has a lower computational cost compared with LES while still resolving approximately 40% of the turbulent friction enhancement. However, modeling approximations are required for unclosed terms. While preliminary models were sufficient to demonstrate the basic concept of TRIS, further spectral analysis of the results highlighted inaccuracies in some of the Reynolds stresses, particularly the wall-normal velocity variance and Reynolds shear stress. This work aims to analyze the dynamics of the Reynolds stresses as resolved by instantaneous wall-normal integrals, particularly the role of unclosed terms. This analysis will involve evaluating terms in the applicable transport equations and comparing model approximations with data from direct numerical simulations. The analysis will provide a detailed account of the inaccuracies of current models in order to gain insight for improving their accuracy.

INTRODUCTION

Prediction of wall-bounded turbulence at high Reynolds number has been a long-standing challenge in the realm of computational approaches. Reynolds-Averaged Navier-Stokes (RANS) provides information on the average flow field, but is incapable of resolving any of the turbulent fluctuations. Alternatively, Large-Eddy Simulation (LES) and Direct Numerical Simulation (DNS) can resolve the large-scale turbulent fluctuations and all of the turbulent fluctuations down to the Kolmogorov length scale, respectively. However, at a high and practical Reynolds number range, the computational cost restricts the applicability of DNS and even wall-model LES as well as hybrid RANS-LES methods (Yang & Griffin, 2021; Goc *et al.*, 2020). This constraining tradeoff between computing power and physical accuracy motivates additional predictive approaches to resolve turbulent fluctuations at a low computational cost for high Reynolds number applications.

Recently, Ragan *et. al.* developed the modeling framework, Turbulence-Resolving Integral Simulation (TRIS), to encapsulate the effects of the large-scale motions (LSMs) and very-large-scale motions (VLSMs) using instantaneous wall-normal integrals (Ragan *et al.*, 2025). It was shown that TRIS is capable of self-sustaining turbulence while capturing the qualitative features of instantaneous flow structures observed in DNS (under wall-normal integration and wall-parallel filtering). It has additionally been emphasized that the computational cost of TRIS is significantly cheaper compared to DNS. For instance, at friction Reynolds number of $Re_\tau = 395$, to run one large-eddy turnover time, the cost of DNS is ~ 100 core-hrs whereas the cost of TRIS is ~ 0.01 core-hrs. Under further inspection, it is shown that the size of the wall-normal velocity structures in TRIS are smaller compared to that in DNS. Two-dimensional spectral analysis shows how TRIS overpredicts the resolved wall-normal velocity at higher wavenumbers (Ragan *et al.*, 2025). This discrepancy directly overlaps with the comparison of the resolved Reynolds shear stress, an important quantity of interest for measuring the skin friction. In essence, TRIS with the original closure approximations is not accurately capturing the mechanism of how energy is transferred from the forcing that drives the flow.

In order for TRIS to become a robust predictive tool for real engineering applications, modeling improvements are necessary. This work will perform a spectral analysis on the transport of the resolved Reynolds stresses using data from DNS at friction Reynolds numbers of $Re_\tau = 180, 395$, and 590. This analysis is similar to that of Lee & Moser (2019), except that the present work will study two-dimensional, three-component vector fields resulting from a wall-normal integrated representation of the flow. Understanding the mechanisms of turbulent production, dissipation, and transfer in the context of instantaneous wall-normal integrals will provide insight on modeling TRIS.

THEORY

This analysis is based on the open-channel flow configuration, where the variables $[x_1, y, x_2] = [x, y, z]$ and $[u_1, v, u_2] = [u, v, w]$ corresponds to the streamwise, wall-normal, and spanwise components of position and velocity, respectively. Here, position and velocity are normalized by the height of the open-channel, h, and friction velocity, u_τ, respectively. So, index notation spans over $j = 1, 2$ such that implied summation applies to the wall-parallel directions only. The bottom wall ($y = 0$) contains a no-slip and no-penetration boundary condition whereas no-slip and no-vorticity boundary conditions are enforced at the top wall ($y = 1$). The boundary conditions for the streamwise and spanwise directions are periodic.

The zeroth and first integral moment operators of any flow variable are defined as

$$\langle\phi\rangle_0 = \int_0^1 \phi dy, \qquad \langle\phi\rangle_1 = \int_0^1 2y\phi dy, \tag{1}$$

respectively. For demonstrative purposes, the transport equations of the resolved (by the zeroth integral moment) Reynolds stresses, $\langle\widetilde{\phi}\rangle_0'\langle\widetilde{\psi}\rangle_0'$, are presented. Here, $\phi' = \phi - \overline{\phi}$, where $\overline{\phi}$ is the Reynolds averaging operator, and $\widetilde{\phi}$ is the wall-parallel filtering operator. The filtering operator is a spectral cutoff filter at $k_{x,\text{cut}} = k_{z,\text{cut}} = 16$, where k_x and k_z are the dimensionless wavenumbers (normalized by h). The effects of wall-parallel spatial filtering is studied in more detail by Ragan *et al.* (2026). The quantities of interest are $\langle\widetilde{u_j}\rangle_0'\langle\widetilde{u_k}\rangle_0'$, $\langle\widetilde{u_j}\rangle_0'\langle\widetilde{v}\rangle_0'$, and $\langle\widetilde{v}\rangle_0'\langle\widetilde{v}\rangle_0'$. Computing the terms in the transport equations for $\langle\widetilde{\phi}\rangle_0'\langle\widetilde{\psi}\rangle_0'$ spectrally pinpoints at which length scales sources and sinks occur via different physical processes. So, to analyze the spectral budget of the resolved Reynolds stresses, Equation (1) (left) must be applied to conservation of momentum, followed by employing the Fourier transform operator, $\widehat{\phi}$, applied in the wall-parallel directions. Then, the velocity (co-)spectra is obtained by computing the following,

$$\frac{\partial\langle\widehat{\widetilde{\phi}}\rangle_0^*\langle\widehat{\widetilde{\psi}}\rangle_0}{\partial t}(k_x,k_z) = \langle\widehat{\widetilde{\phi}}\rangle_0^*\frac{\partial\langle\widehat{\widetilde{\psi}}\rangle_0}{\partial t} + \langle\widehat{\widetilde{\psi}}\rangle_0\frac{\partial\langle\widehat{\widetilde{\phi}}\rangle_0^*}{\partial t}, \tag{2}$$

where ϕ^* is the complex conjugate of the Fourier transform. The signal is split by the following, $\phi^*\psi = \mathscr{R}\{\phi^*\psi\} + \mathscr{I}\{\phi^*\psi\}$, where the first and second term considers the real and imaginary component of the signal, respectively. This paper will only consider the real part of the signal since it is the only component to contribute towards net momentum transport. First, the spectral budget of the resolved wall-parallel stresses is provided,

$$\begin{aligned}\frac{\partial\langle\widehat{\widetilde{u_j}}\rangle_0^*\langle\widehat{\widetilde{u_k}}\rangle_0}{\partial t} &= \mathscr{R}\Big\{\underbrace{-i\kappa_l\langle\widehat{\widetilde{u_j}}\rangle_0^*\langle\widehat{\widetilde{u_k u_l}}\rangle_0 - \langle\widehat{\widetilde{u_k}}\rangle_0\left(i\kappa_l\langle\widehat{\widetilde{u_j u_l}}\rangle_0\right)^*}_{A_0(u_j,u_k)} \\ &\underbrace{-i\kappa_k\langle\widehat{\widetilde{u_j}}\rangle_0^*\langle\widehat{\widetilde{p}}\rangle_0 - \langle\widehat{\widetilde{u_k}}\rangle_0\left(i\kappa_j\langle\widehat{\widetilde{p}}\rangle_0\right)^*}_{P_0(u_j,u_k)} \\ &\underbrace{-2\frac{\kappa_l\kappa_l}{Re_\tau}\langle\widehat{\widetilde{u_j}}\rangle_0^*\langle\widehat{\widetilde{u_k}}\rangle_0 - \left[\langle\widehat{\widetilde{u_j}}\rangle_0^*\widehat{\widetilde{\tau}}_k + \langle\widehat{\widetilde{u_k}}\rangle_0\widehat{\widetilde{\tau}}_j^{\,*}\right]}_{V_0(u_j,u_k)}\Big\},\end{aligned} \tag{3}$$

where the parameters, i, p, and τ_j, are the imaginary unit, pressure, and instantaneous wall shear stress, respectively. The first row of Equation (3) represents advection by the zeroth moment of velocity and the second row captures the effects of the pressure/strain-rate correlation. The first and second terms in the third row are sinks of viscous dissipation and wall shear stress, respectively. The evolution equation for the resolved Reynolds shear stress is presented,

$$\begin{aligned}\frac{\partial\left(-\langle\widehat{\widetilde{u_j}}\rangle_0^*\langle\widehat{\widetilde{v}}\rangle_0\right)}{\partial t} &= \mathscr{R}\Big\{\underbrace{i\kappa_l\langle\widehat{\widetilde{u_j}}\rangle_0^*\langle\widehat{\widetilde{v u_l}}\rangle_0 + \langle\widehat{\widetilde{v}}\rangle_0\left(i\kappa_l\langle\widehat{\widetilde{u_j u_l}}\rangle_0\right)^*}_{A_0(u_j,v)} \\ &+\underbrace{\langle\widehat{\widetilde{u_j}}\rangle_0^*\,\widehat{\widetilde{p}}\Big|_{y=0}^{y=1} + \langle\widehat{\widetilde{v}}\rangle_0\left(i\kappa_j\langle\widehat{\widetilde{p}}\rangle_0\right)^*}_{P_0(u_j,v)} \\ &\underbrace{+2\frac{\kappa_l\kappa_l}{Re_\tau}\langle\widehat{\widetilde{u_j}}\rangle_0^*\langle\widehat{\widetilde{v}}\rangle_0 - \frac{\langle\widehat{\widetilde{u_j}}\rangle_0^*}{Re_\tau}\frac{\partial\widehat{\widetilde{v}}}{\partial y}\Big|_{y=1} + \langle\widehat{\widetilde{v}}\rangle_0\widehat{\widetilde{\tau}}_j^{\,*}}_{V_0(u_j,v)}\Big\}.\end{aligned} \tag{4}$$

In Equation (4), the first and second rows represents advection and pressure/strain-rate correlation of the resolved stress, respectively. Due to the wall-normal integration, the first term in the second row considers the effects of pressure at the wall boundaries. The third row captures the viscous dissipation, where the second term includes dissipation at the top wall boundary. The final row is a sink by the wall shear stress. Lastly, the resolved wall-normal component of the Reynolds stress is presented,

$$\begin{aligned}\frac{\partial\langle\widehat{\widetilde{v}}\rangle_0^*\langle\widehat{\widetilde{v}}\rangle_0}{\partial t} = -2\mathscr{R}\Bigg\{&\underbrace{i\kappa_l\langle\widehat{\widetilde{v}}\rangle_0^*\langle\widehat{\widetilde{v u_l}}\rangle_0}_{A_0(v,v)} - \underbrace{\langle\widehat{\widetilde{v}}\rangle_0^*\,\widehat{\widetilde{p}}\Big|_{y=0}^{y=1}}_{P_0(v,v)} \\ &+\underbrace{\frac{\kappa_l\kappa_l}{Re_\tau}\langle\widehat{\widetilde{v}}\rangle_0^*\langle\widehat{\widetilde{v}}\rangle_0 - \frac{\langle\widehat{\widetilde{v}}\rangle_0^*}{Re_\tau}\frac{\partial\widehat{\widetilde{v}}}{\partial y}\Big|_{y=1}}_{V_0(v,v)}\Bigg\}.\end{aligned} \tag{5}$$

The first and second terms of Equation (5) are advection and pressure/strain-rate correlation effects, respectively. The third and fourth term captures the viscous dissipation. For Equations (3)-(5), $A_0(\phi,\psi)$, $P_0(\phi,\psi)$, and $V_0(\phi,\psi)$ represents the advection, pressure/strain-rate correlation, and viscous dissipation/wall shear stress terms, respectively. Specifically, $A_0(u_j,u_k)$, $P_0(u_j,u_k)$, and $V_0(u_j,u_k)$ correspond to Equation (3), $A_0(u_j,v)$, $P_0(u_j,v)$, and $V_0(u_j,u_k)$ refer to Equation (4), and $A_0(v,v)$, $P_0(v,v)$, and $V_0(v,u_k)$ relate to Equation (5). The variables that require models for closure include $\langle\widetilde{u_j u_k}\rangle_0$, $\langle\widetilde{v u_j}\rangle_0$, τ_j, $p|_{y=0}^{y=1}$, and $\partial\widetilde{v}/\partial y(y=1)$.

By including the first integral moment, TRIS is able to self-sustain turbulence because the wall-normal component of velocity is obtained, e.g., applying Equation (1) (right) to mass conservation gives $\partial\langle\widetilde{u_i}\rangle_1/\partial x_i = 2\langle\widetilde{v}\rangle_0$. Therefore, it is equally imperative to assess the wall-parallel velocity components resolved by the first integral moment. Following a similar approach to computing the resolved Reynolds stresses by the zeroth integral moment, the resolved wall-parallel stresses by the first integral moment can be derived,

$$\begin{aligned}\frac{\partial\langle\widehat{\widetilde{u_j}}\rangle_1^*\langle\widehat{\widetilde{u_k}}\rangle_1}{\partial t} &= \mathscr{R}\Big\{\underbrace{-i\kappa_l\langle\widehat{\widetilde{u_j}}\rangle_1^*\langle\widehat{\widetilde{u_k u_l}}\rangle_1 - \langle\widehat{\widetilde{u_k}}\rangle_1\left(i\kappa_l\langle\widehat{\widetilde{u_j u_l}}\rangle_1\right)^*}_{A_1(u_j,u_k)} \\ &+\underbrace{2\left[\langle\widehat{\widetilde{u_j}}\rangle_1^*\langle\widehat{\widetilde{u_k v}}\rangle_0 + \langle\widehat{\widetilde{u_k}}\rangle_1\langle\widehat{\widetilde{u_j v}}\rangle_0^*\right]}_{T_1(u_j,u_k)} \\ &\underbrace{-i\kappa_k\langle\widehat{\widetilde{u_j}}\rangle_1^*\langle\widehat{\widetilde{p}}\rangle_1 - \langle\widehat{\widetilde{u_k}}\rangle_1\left(i\kappa_j\langle\widehat{\widetilde{p}}\rangle_1\right)^*}_{P_1(u_j,u_k)} \\ &\underbrace{-2\frac{\kappa_l\kappa_l}{Re_\tau}\langle\widehat{\widetilde{u_j}}\rangle_1^*\langle\widehat{\widetilde{u_k}}\rangle_1 - \frac{2}{Re_\tau}\left[\langle\widehat{\widetilde{u_j}}\rangle_1^*\widehat{\widetilde{u}}_{k,top} + \langle\widehat{\widetilde{u_k}}\rangle_1\widehat{\widetilde{u}}_{j,top}^{\,*}\right]}_{V_1(u_j,u_k)}\Big\},\end{aligned} \tag{6}$$

where $u_{j,\text{top}}$ is the velocity at the top wall ($y=1$). In Equation (6), the first, second, and third rows correspond to advection ($A_1(\phi,\psi)$), effects by the Reynolds shear stress ($T_1(\phi,\psi)$), and pressure/strain-rate correlation ($P_1(\phi,\psi)$), respectively. The fourth and fifth rows denote viscous dissipation and effects by the top wall, respectively, and are represented by $V_1(\phi,\psi)$. Additional variables from Equation (6) such as $\langle\widetilde{u_j u_k}\rangle_1$ and $u_{j,\text{top}}$ require closure models.

SIMULATION DATASET

The open-channel flow data used in this analysis is gathered from the DNS code developed by Lozano-Durán *et al.* (2018). Here, a second-order central differencing scheme is computed on a staggered grid, and time is advanced using an explicit third-order Runge-Kutta scheme. The domain size in the streamwise and spanwise directions are 8π and 3π, respectively, with a channel height set to unity. The criteria for the grid discretizations (in inner units, denoted by the superscript "+") are $\Delta x^+ \lesssim 7.0$, $\Delta z^+ \lesssim 6.0$, $\Delta y_w^+ \lesssim 0.35$, and $\Delta y_{max}^+ \lesssim 6.0$, where Δy_w^+, and Δy_{max}^+ are the grid spacing nearest and farthest from the bottom wall (y=0), respectively.

Data is collected for Reynolds numbers at $Re_\tau = 180, 395$, and 590, where 40 snapshots across 40 large-eddy turnover times are gathered for $Re_\tau = 180$ and 590 and 200 snapshots across 20 large-eddy turnover times are gathered for $Re_\tau = 395$. The DNS methodology was first verified by comparing one-point statistics of the full-channel flow against Moser *et al.* (1999), then the discretization was extended to the open-channel flow configuration (see Appendix A in Ragan *et al.* (2025)).

REYNOLDS-AVERAGED BUDGET

The Reynolds-averaged values of the source/sink terms across Equations (3)-(5) are computed, as shown in Table 1. According to the top row of Table 1, the resolved streamwise velocity variance dominates compared to the spanwise and wall-normal components. The "$-uv$" column computes quantities such that positive and negative values are sources and sinks of the negative co-variance, respectively. The second row is the numerical value of the largest source term and the following three rows contain values in bold that correspond to the source of the resolved Reynolds stress. The final row computes the percent residual of the Reynolds-averaged budget equation to ensure the statistical convergence criteria is satisfied. As expected, with increasing Re_τ values, the $V_0(\phi,\psi)$ term becomes noticeably weaker. So, at high Reynolds number flows, the advection and pressure effects become the dominant sources and sinks, with presumably weak effects of the wall shear stress sink term in Equations (3) and (4).

For $\phi\psi = uu$, production occurs in the advection term, $A_0(u,u)$, while $\sim 63\%$ of destruction occurs in the pressure term, $P_0(u,u)$. For $\phi\psi = ww$, production resides in $P_0(w,w)$, caused by the pressure redistribution from $P_0(u,u)$. The relationship between $P_0(u,u)$ and $P_0(w,w)$ is established by applying Equation (1) (left) to mass conservation,

$$\overline{\langle\widetilde{p}\rangle_0' \frac{\partial\langle\widetilde{u}\rangle_0'}{\partial x}} + \overline{\langle\widetilde{p}\rangle_0' \frac{\partial\langle\widetilde{w}\rangle_0'}{\partial z}} = 0. \qquad (7)$$

The primary sink of $\langle\widetilde{w}\rangle_0'\langle\widetilde{w}\rangle_0'$ is caused by the advection, $A_0(w,w)$. Regarding $\phi\psi = vv$, the production of $\langle\widetilde{v}\rangle_0'\langle\widetilde{v}\rangle_0'$ comes from the advection term, $A_0(v,v)$. Due to the lower magnitude of the source term, the viscous diffusion term, $V_0(v,v)$ decays with respect to Re_τ at a noticeably slower rate compared to the other Reynolds stress components. Lastly, production of $-\langle\widetilde{u}\rangle_0'\langle\widetilde{v}\rangle_0'$ resides in $A_0(u,v)$, while the primary sink lies in $P_0(u,v)$. This shows that the advection term is responsible for both adding streamwise fluctuation energy via interaction with (unresolved) mean shear and removing energy via spanwise diffusion.

Table 2 records the Reynolds-averaged values of the sources and sinks of Equation (6). The $\langle\widetilde{u}\rangle_1'\langle\widetilde{u}\rangle_1'$ fluctuations are mainly balanced out by the advection term ($A_1(u,u)$) and effects by the Reynolds shear stress term ($T_1(u,u)$). In fact, $\sim 93\%$ of the source for $\phi\psi = uu$ is destroyed by $T_1(u,u)$. The pressure/strain-rate correlation and viscous dissipation with effects by the top wall ($P_1(u,u)$ and $V_1(u,u)$, respectively) contributes to the remaining 7%. For the $\langle\widetilde{w}\rangle_1'\langle\widetilde{w}\rangle_1'$ fluctuations, production occurs in the pressure/strain-rate correlation, $P_1(w,w)$, and is removed by the advection term, $A_1(w,w)$. The remaining terms contribute $5-7\%$ of the production term, with 2% error. According to the following relationship derived from applying Equation (1) (right) the mass conservation,

$$\overline{\langle\widetilde{p}\rangle_1' \frac{\partial\langle\widetilde{u}\rangle_1'}{\partial x}} + \overline{\langle\widetilde{p}\rangle_1' \frac{\partial\langle\widetilde{w}\rangle_1'}{\partial z}} = 2\overline{\langle\widetilde{v}\rangle_0'\langle\widetilde{p}\rangle_1'}, \qquad (8)$$

$P_1(u,u)$ is split into $P_1(w,w)$ and the $\langle\widetilde{v}\rangle_0'\langle\widetilde{p}\rangle_1'$ correlation.

SPECTRAL BUDGET

In this section, the significant terms of Equations (3)-(5), are analyzed *a priori* in wavenumber space. Since $V_0(\phi,\psi)$ is relatively weak according to Table 1, comparisons between $A_0(\phi,\psi)$ and $P_0(\phi,\psi)$ terms are highlighted, with the exception of $V_0(v,v)$. Results are presented at $Re_\tau = 395$ because the large sample of 200 snapshots provides a means to achieve statistical convergence on the spectral plots. The premultiplied spectra for the primary terms in Equation (3) are illustrated in Figure 1. Here, the resolved streamwise velocity fluctuations are produced by the advection term, $A_0(u,u)$, for $2 \lesssim k_x \lesssim 16$ and $3 \lesssim k_z \lesssim 16$ in Figure 1 (left). As reported in Table 1, 78% of the production of $\langle\widetilde{u}\rangle_0'\langle\widetilde{u}\rangle_0'$ is redistributed by the pressure/strain-rate correlation, i.e., the majority of the resolved streamwise velocity fluctuations sinks in $P_0(u,u)$ (Figure 1, middle). The pressure redistributes to $P_0(w,w)$, which is the source for $\langle\widetilde{w}\rangle_0'\langle\widetilde{w}\rangle_0'$ (Figure 1, right). The length scales at which pressure redistribution occurs are quite similar to the length scale of $A_0(u,u)$. According to Table 1, 97% of the resolved spanwise velocity fluctuations produced from $P_0(w,w)$ is removed by the advection term, $A_0(w,w)$, at the similar wavenumber range mentioned previously (not shown). For the viscous (and wall-shear stress) term, the majority $V_0(u,u)$ occurs for $k_x \lesssim 2$ and $3 \lesssim k_z \lesssim 4$ while $V_0(w,w)$ occurs for $k_x \gtrsim 5$ and $k_z \gtrsim 5$ (not shown).

Figure 2 (top) illustrates the advection term, $A_0(u,v)$, of the resolved Reynolds shear stress, $-\langle\widetilde{u}\rangle_0'\langle\widetilde{v}\rangle_0'$ as a function of wavenumber. According to Table 1, $A_0(u,v)$ is the production term that occurs at $4 \lesssim k_x \lesssim 16$ and $3 \lesssim k_z \lesssim 16$. Furthermore, 95% of the $-\langle\widetilde{u}\rangle_0'\langle\widetilde{v}\rangle_0'$ produced is removed by the pressure/strain-rate correlation, $P_0(u,v)$. Destruction occurs at a similar wavenumber range where production occurs (see Figure 2, bottom). The rest of the resolved Reynolds shear stress is removed by $V_0(u,v)$ at relatively high spanwise wavenumbers, $2 \lesssim k_x \lesssim 16$ and $8 \lesssim k_z \lesssim 16$ (not shown).

Results for the spectral balance of $\langle\widetilde{v}\rangle_0'\langle\widetilde{v}\rangle_0'$ requires more snapshots for statistical convergence. However, general observations suggest that activity of production ($A_0(v,v)$) and destruction ($P_0(v,v)$ and $V_0(v,v)$) is observed at high wavenumbers of roughly $k_x \gtrsim 5$ and $k_z \gtrsim 4$ (not shown). Interestingly, it appears that the current spectral cutoff filter at $k_{x,\mathrm{cut}} = k_{z,\mathrm{cut}} = 16$ is removing this high wavenumber activity. Using this cutoff filter, Ragan *et al.* (2026) showed that TRIS can theoretically capture 74% of the of the resolved and unfiltered wall-normal velocity fluctuations, i.e, $\overline{\langle\widetilde{v}\rangle_0'\langle\widetilde{v}\rangle_0'}/\overline{\langle v\rangle_0'\langle v\rangle_0'} = 74\%$. If the grid resolution in the streamwise and spanwise directions were to double ($k_{x,\mathrm{cut}} = k_{z,\mathrm{cut}} = 32$), then 92% of $\overline{\langle v\rangle_0'\langle v\rangle_0'}$ is captured. Therefore, a finer grid in TRIS may be able to better represent the time evolution of the resolved wall-normal velocity fluctuations.

Since Table 2 shows how the source of $\phi\psi = uu$ dominates the source of $\phi\psi = ww$ and how viscous effects play

Table 1: Reynolds averaged values of the resolved Reynolds stresses as well as the advection, pressure/strain-rate correlation, and viscous dissipation/wall shear stress terms ($A_0(\phi,\psi)$, $P_0(\phi,\psi)$, and $V_0(\phi,\psi)$, respectively) normalized by the source term in Equations (3)-(5). Values in bold correspond to the source of the resolved Reynolds stress.

Re_τ	180				395				590			
$\phi\psi$	uu	ww	vv	$-uv$	uu	ww	vv	$-uv$	uu	ww	vv	$-uv$
$\overline{\langle\widetilde{\phi}\rangle'_0\langle\widetilde{\psi}\rangle'_0}$	0.76	0.12	0.14	0.19	0.73	0.11	0.14	0.19	0.77	0.11	0.13	0.18
source	1.54	0.97	0.17	1.16	1.28	1.00	0.12	1.29	1.20	0.98	0.09	1.24
$\overline{A_0(\phi,\psi)}$/source	**1.00**	-0.96	**1.00**	**1.00**	**1.00**	-0.97	**1.00**	**1.00**	**1.00**	-0.98	**1.00**	**1.00**
$\overline{P_0(\phi,\psi)}$/source	-0.63	**1.00**	-0.29	-0.86	-0.78	**1.00**	-0.48	-0.95	-0.82	**1.00**	-0.56	-0.96
$\overline{V_0(\phi,\psi)}$/source	-0.35	-0.06	-0.75	-0.12	-0.21	-0.03	-0.53	-0.05	-0.18	-0.02	-0.44	-0.04
Residual	0.02	-0.02	-0.04	0.02	0.01	0.00	-0.01	0.00	0.00	0.00	0.00	0.00

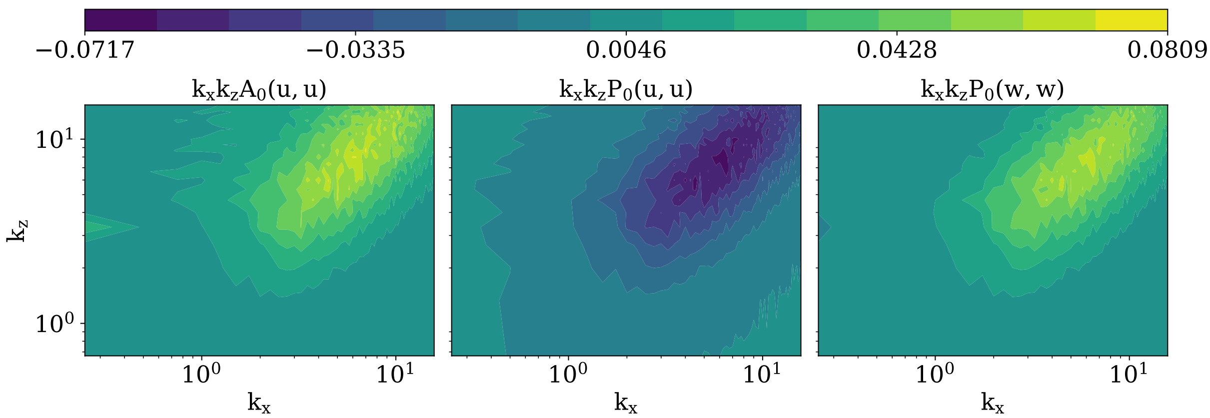

Figure 1: Pre-multiplied two-dimensional spectra of the advection term, $A_0(u,u)$ (left), and pressure terms, $P_0(u,u)$ (middle) and $P_0(w,w)$ (right), in Equation (3). Results are plotted at $Re_\tau = 395$.

Table 2: Values for the advection ($A_1(\phi,\psi)$), effects by the Reynolds shear stress ($T_1(\phi,\psi)$), pressure/strain-rate correlation ($P_1(\phi,\psi)$), and viscous dissipation ($V_1(\phi,\psi)$) terms in Equation (6). Results are reported at $Re_\tau = 395$ and values in bold correspond to the source term.

$\phi\psi$	uu	ww
source	12.19	0.61
$\overline{A_1(\phi,\psi)}$/source	**1.00**	-0.95
$\overline{T_1(\phi,\psi)}$/source	-0.93	0.00
$\overline{P_1(\phi,\psi)}$/source	-0.06	**1.00**
$\overline{V_1(\phi,\psi)}$/source	-0.01	-0.07
Residual	0.00	-0.02

a negligible role at $Re_\tau = 395$, the spectral balance between the advection term, $A_1(u,u)$, and effects by the turbulent stress, $T_1(u,u)$, roughly summarizes the transport of the wall-parallel stresses resolved by the first integral moment. Figure 3 (top) illustrates the spectral distribution of the advection term, $A_1(u,u)$, in Equation (6). Production of $\langle\widetilde{u}\rangle'_1\langle\widetilde{u}\rangle'_1$ contains two peaks. One peak is located at $kx \approx 0.2$ and $kx \approx 3-4$, corresponding to long and streaky structures. The other peak is located at $kx \approx 3$ and $kx \approx 6$, representing production of smaller structures. The destruction of $\langle\widetilde{u}\rangle'_1\langle\widetilde{u}\rangle'_1$ by $T_1(u,u)$ as a function of wavenumber is observed in Figure 3 (bottom). Here, the sink occurs at a similar wavenumber range as $A_1(u,u)$.

MODELING IMPLEMENTATION

Further comparison between DNS and TRIS shows that the highest discrepancy is located in the transport of the resolved Reynolds shear stress, Equation (4). Specifically, the first term of $A_0(u_j,v)$, $(\langle\widetilde{u_j}\rangle'_0\partial\langle\widetilde{vu_k}\rangle'_0/\partial x_k)$, is computed as a source in DNS. On the contrary, this term is computed as a sink in TRIS. This qualitative error motivates a better model for $\langle\widetilde{u_jv}\rangle_0$. This unclosed term is decomposed into the following,

$$\langle\widetilde{u_jv}\rangle_0 = \langle\widetilde{u_j}\rangle_0\langle\widetilde{v}\rangle_0 + \langle\widetilde{u''_jv''}\rangle_0, \tag{9}$$

where the first and second terms are the components that are resolved and unresolved by the zeroth integral moment, respectively. The unresolved turbulent shear stress is modeled using an eddy viscosity approximation (Smagorinsky, 1963),

$$\langle\widetilde{u''_jv''}\rangle_0 = \int_0^1 \nu_T\left(\frac{\partial\widetilde{u_j}}{\partial y} + \frac{\partial\widetilde{v}}{\partial x_j}\right)dy, \tag{10}$$

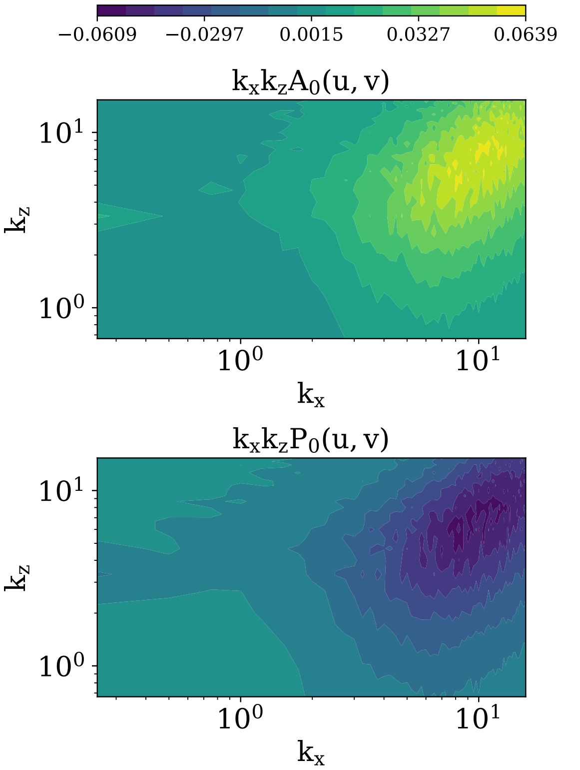

Figure 2: Pre-multiplied two-dimensional spectra of the advection term, $A_0(u,v)$ (top) and pressure term, $P_0(u,v)$ (bottom), in Equation (4). Results are plotted at $Re_\tau = 395$.

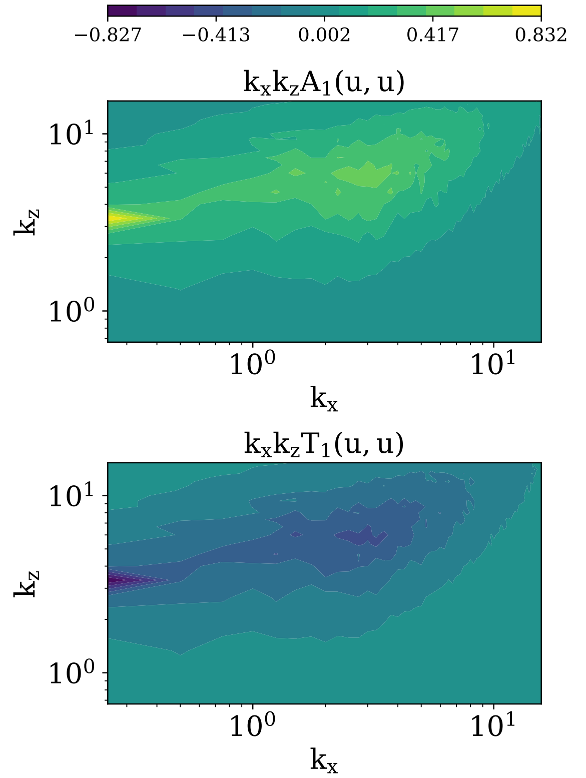

Figure 3: Pre-multiplied two-dimensional spectra of the advection term, $A_1(u,u)$ (top) and effects by the Reynolds shear stress term, $T_1(u,u)$ (bottom), in Equation (6). Results are plotted at $Re_\tau = 395$.

where $\nu_T = C_T\kappa y$ is the eddy viscosity coefficient with wall-normal scaling, C_T is a set model coefficient based on the unresolved Reynolds shear stress (see Appendix B in Ragan *et al.* (2025)), and $\kappa = 0.41$ is the inverse log slope of the Coles profile. The first term on the right-hand-side of Equation (10) applies wall-normal diffusion whereas the second term applies wall-parallel diffusion to the unresolved stress. For simplicity, Ragan *et al.* (2025) neglects the second term in Equation (10). For the purpose of improving the closure model for $\langle\widetilde{u_j v}\rangle_0$, this neglected term is reintroduced,

$$C_T\kappa\frac{\partial}{\partial x_j}\left(\int_0^1 y\tilde{v}dy\right) = \frac{1}{2}C_T\kappa\frac{\partial\langle\tilde{v}\rangle_1}{\partial x_j} \approx C_v\frac{\partial\langle\tilde{v}\rangle_0}{\partial x_j}, \qquad (11)$$

where it is assumed that the $\langle\tilde{v}\rangle_1 = \alpha\langle\tilde{v}\rangle_0$, α is some constant coefficient, and $C_v = C_T\kappa\alpha/2$. The results of this paper are presented with the tuned coefficient of $C_v = 0.01$. Additionally, the strength of $\langle\widetilde{u_j u_k}\rangle_0$ and $\langle\widetilde{u_j u_k}\rangle_1$ that is resolved by the structural model is artificially increased by 9% for the purpose of maintaining proper balance of the resolved and unresolved turbulent shear stress. Briefly, the structural model involves employing an assumed skewed Coles velocity profile (Coles, 1956). Further detail on the modeling implementation and criteria for TRIS is found in Ragan *et al.* (2025). In general, the modifications made to TRIS are the following, (i) implementing wall-parallel diffusion to the turbulent shear stress and (ii) increasing the strength of the wall-parallel stresses resolved by the structural model by 9%. With these modifications, the first term of $A_0(u,v)$ is now computed as a source, which reflects the same behavior illustrated in DNS.

Additional performance of the model is illustrated in Figure 4, where "Original TRIS" corresponds to the model used in Ragan *et al.* (2025), "Updated TRIS" corresponds to the closure model with modifications, and "DNS" corresponds to the reference data. These results are denoted by light-dashed lines, dark-dashed lines, and dark-solid lines, respectively. The red and blue curves represent the streamwise and spanwise spectral distributions, respectively. The original TRIS model is capable of capturing the general trend of this model. On the other hand, the updated TRIS model matches well with DNS for $k_x \lesssim 3$, but then appears to drop off after the fact, most likely due to the inclusion of the wall-parallel eddy viscosity on the resolved Reynolds shear stress. DNS shows that the maximum value for the spectral distribution of $-k_z\mathscr{R}\{\langle\widehat{u}\rangle_0\langle\widehat{v}\rangle_0^*\}$ in the spanwise direction is located at $k_z \sim 4$. The original TRIS model has this maximum located at the highest wavenumber with an additional underprediction at the lowest wavenumber. The new TRIS model, alternatively, captures the trend in DNS quite nicely.

The one-dimensional spectral distribution of the resolved streamwise velocity spectra is illustrated in Figure 4 (middle). Here, data from DNS shows that the peaks of these distributions occur at $k_x = 1/4$ (the lowest wavenumber) and $k_z \sim 4$. The old TRIS model shows under-prediction at all wavenumbers, this applies to both the streamwise and spanwise directions. However, the modified TRIS model shows better prediction for $k_x \lesssim 3$ with a significant dropoff for $k_x \gtrsim 3$ and nice alignment for the k_z spectra.

Lastly, the wall-normal velocity spectra is plotted in Figure 4 (bottom). According to DNS, the peaks of the spectra occur at $k_x = k_z \sim 7$, which is at a higher location compared to the other components. The spectra from the unmodified TRIS solver show these peaks occurring at the highest wavenumber values in both the streamwise and spanwise directions. The

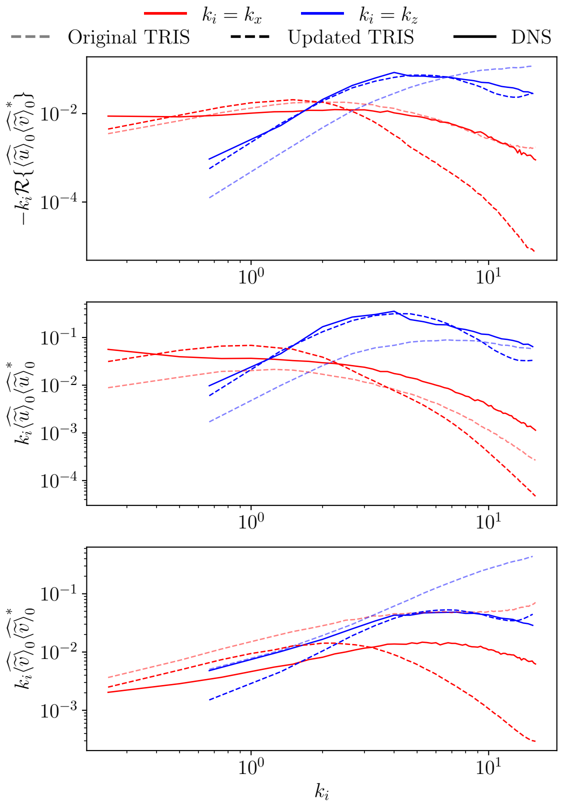

Figure 4: Pre-multiplied one-dimensional spectra of the integral-resolved streamwise and spanwise velocity fluctuations as well as the co-variance. Results are plotted at $Re_\tau = 395$.

updated TRIS fixes this error, but the peaks of the streamwise spectra occur at $k_x \sim 1$, showing that the spectra drops off sooner than necessary. On the other hand, the peak of the spanwise spectra occurs at $k_z \sim 7$, as needed. However, the modified TRIS now underpredicts the spanwise spectra at lower wavenumbers (for $k_z \lesssim 4$).

CONCLUSION

With its potential savings in computational cost, TRIS has the capability to serve as an excellent tool for predicting wall-bounded turbulent flows. Although it is capable of capturing general behavior of instantaneous wall-normal integrated flows, TRIS illustrated excessive magnitude of wall-normal velocity fluctuations at the smallest length scale. To suppress this discrepancy, *a priori* analysis of the resolved Reynolds stress transport is performed to target better closure approximation. It turns out that terms possessing $\langle \widetilde{vu_j} \rangle_0$ across Equations (3)-(6) are quite influential with respect to how the resolved Reynolds stresses evolve in time. Additional analysis on the spectral budget for the resolved wall-normal velocity suggests that a slightly finer grid may be beneficial to capture the dynamics of this component.

According to DNS, the advection of the $\langle \widetilde{vu_j} \rangle_0'$ by $\langle \widetilde{u} \rangle_0$ serves as production of the resolved turbulent stress (first term of $A_0(u,v)$ in Equation (4)). However, TRIS computed this term as a sink. This observation motivated the need to improve the $\langle \widetilde{vu_j} \rangle_0$ closure. In particular, implementing wall-parallel diffusion to the unresolved Reynolds shear stress (and increasing the strength of the structural model) fixed this qualitative discrepancy. Further comparison illustrates better alignment of the resolved (co-)spectra in the k_z direction. Excessive suppression of the resolved stresses at higher k_x values has also been observed as a result of the modifications made to the TRIS closure models (future work aims to fix this feature). Even so, relaxing these stresses at the smallest scales allow for grid convergence to be attainable in TRIS.

This improvement is one example of how spectral analysis on the budget equation for the resolved Reynolds stresses can benefit the TRIS closure models. More observations on these spectra can be made to target improvements on other unclosed terms in TRIS. For instance, a more robust approach can be made to substitute the artificial increase of the structural model of the zeroth and first integral moment of the wall-parallel stresses ($\langle \widetilde{u_j u_k} \rangle_0$ and $\langle \widetilde{u_j u_k} \rangle_1$, respectively).

ACKNOWLEDGMENT

TR was supported by the Department of Defense (DoD) through the National Defense Science & Engineering Graduate (NDSEG) Fellowship Program. PJ was supported by the National Science Foundation under CAREER award No. 2340121. The authors acknowledge the DoD High Performance Computing Modernization Program (HPCMP) for providing the computing resources for this analysis.

REFERENCES

Coles, Donald 1956 The law of the wake in the turbulent boundary layer. *J. Fluid Mech.* **1** (2), 191–226.

Goc, K., Bose, S. & Moin, P. 2020 Wall-modeled large eddy simulation of an aircraft in landing configuration. In *AIAA Aviation 2020 Forum*, p. 3002.

Lee, Myoungkyu & Moser, Robert D. 2019 Spectral analysis of the budget equation in turbulent channel flows at high reynolds number. *J. Fluid Mech.* **860**, 886–938.

Lozano-Durán, A., Hack, M. J. P. & Moin, P. 2018 Modeling boundary-layer transition in direct and large-eddy simulations using parabolized stability equations. *Phys. Rev. Fluids* **3**, 023901.

Moser, Robert D, Kim, John & Mansour, Nagi N 1999 Direct numerical simulation of turbulent channel flow up to reτ= 590. *Physics of fluids* **11** (4), 943–945.

Ragan, Tanner, Warnecke, Mark & Johnson, Perry L. 2026 Effects of spatial filtering on instantaneous wall-normal integrals for turbulent channel flows. *AIAA Journal* (Published online: 10.2514/1.J066041).

Ragan, Tanner, Warnecke, Mark, Stout, Samuel Tomaras & Johnson, Perry 2025 Turbulence-resolving integral simulations for wall-bounded flows. *Journal of Fluid Mechanics* **1014**, A40.

Smagorinsky, J. 1963 General circulation experiments with the primitive equations: I. the basic experiment. *Monthly Weather Review* **91** (3), 99 – 164.

Yang, X. I. A. & Griffin, K. P. 2021 Grid-point and time-step requirements for direct numerical simulation and large-eddy simulation. *Phys. Fluids* **33** (1), 015108.